OptoSkin: Novel LIDAR Touch Sensors for Detection of Touch and Pressure within Wave guides

Emmanuel Bacher, Sergio Cartiel, Jorge García-Pueyo, Julija Stopar, Aleš Zore, Roman Kamnik, Ilze Aulika, Andrejs Ogurcovs, Jurģis Grūbe, Arturs Bundulis, Jelena Butikova, Meldra Kemere, Adolfo Muñoz, and Martin Laurenzis

***Abstract*— Light Detection and Ranging (LIDAR) sensors, employing direct Time-of-Flight (dTOF) measurements, are crucial for precise surface localization and are increasingly integrated into compact chip designs. These sensors have extensive use in proximity sensing in various applications. This paper presents the innovative use of LIDAR sensors for ranging within wave guides to accurately detect touch and pressure. In our OptoSkin sensors, light propagates via total internal reflection (TIR) within the wave guide. Then it is reflected back to the sensor as a result of wave guide deformation and/or scattering in the contact area, a phenomenon attributed to frustrated total internal reflection (FTIR). We have designed, simulated, and implemented different OptoSkin sensors using wave guides constructed from a flexible rod, rigid curved 3D printed resin, and planar soft silicone rubber, respectively. Each configuration is equipped with multiple LIDAR sensors, demonstrating effective localization of touch points. In addition, pressure sensing was performed on the elastic wave guides. These novel touch sensors show great potential for applications such as robotic sensor skins, which enhance tactile responsiveness and interaction.**

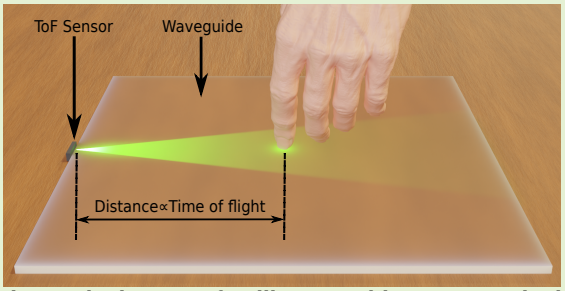

***Index Terms*— Light detection and ranging, LIDAR, Time-of-Flight, TOF, touch detection, tactile sensing, frustrated total internal reflection, FTIR, wave guide, light guide, optical sensing, robotic sensor skin, proximity sensing**

I. Introduction

Frustrated Total Internal Reflection (FTIR) tactile sensors exploit light behaviour to precisely detect touch and pressure. These sensors operate on the principle of light being totally reflected within a transparent medium until an object interferes, facilitating the measurement of touch location, force, and shape. All touch sensors based on FTIR described in the literature exhibit two primary configurations: first, the light detector directly observes the contact point [1]–[7], and second, the light detector laterally observes the contact point [7]–[11] within a defined sensing area. The spatial resolution of these sensors varies from approximately $0.1\,\mathrm{mm}$ to $5\,\mathrm{mm}$, while the sensing area ranges from about $20\,\mathrm{mm} \times 20\,\mathrm{mm}$ to $300\,\mathrm{mm} \times 300\,\mathrm{mm}$, respectively.

These FTIR touch sensor solutions typically require multiple light emitters and receivers to cover relatively large areas. Additionally, some designs necessitate complex material shapes, such as custom-built wedge-shaped optically transparent acrylic prisms to function as optical wave guides [9]. Furthermore, in the case of ToF fiber touch sensors, a complex waveguide configuration is suggested, where one end of the fiber is connected to the ToF light source for input, and the other end serves as output for the ToF detector [11].

Nevertheless, FTIR sensors are highly sensitive and capable of simultaneously detecting multiple touch points and object shapes, making them ideal for applications in robotics for grippers, that require sensor equipment in compact spaces. However, they are sensitive to external light conditions and require controlled environments to avoid calibration issues. The materials used can also limit their effectiveness, and their complex data processing needs can be computationally intensive.

In this paper, we present the OptoSkin sensor, a novel system that merges multiple laser detection and ranging (LiDAR) sensors with a quasi-two-dimensional optical wave guide. Light propagation within this wave guide is based on

All authors contributed equally to the work presented in this paper.

E. Bacher and M. Laurenzis were with the French-German Research Institute of Saint-Louis, 5 rue du Général Cassagnou, BP 70034, 68301 SAINT-LOUIS Cedex, France (e-mail: martin.laurenzis@isl.eu).

S. Cartiel, J. García-Pueyo and A. Muñoz were with the University of Zaragoza and I3A, C. Maria de Luna, 1, 50019 Zaragoza, Spain (e-mail:adolfo@unizar.es)

Ilze Aulika, Andrejs Ogurcovs, Jurģis Grūbe, Arturs Bundulis, Jelena Butikova and Meldra Kemere were with the Institute of Solid State Physics, University of Latvia, Kengaraga 8, LV-1063, Riga, Latvia (e-mail:aulika@cfi.lu.lv)

Julija Stopar, Aleš Zore and Roman Kamnik were with University of Ljubljana, Faculty of Electrical Engineering, Tržaška cesta 25, 1000 Ljubljana, Slovenia (e-mail: roman.kamnik@fe.uni-lj.si)

total internal reflection (TIR). Our method entails conducting range measurements within the wave guide to accurately detect both the position and pressure exerted during tactile interactions, resulting in scattering phenomena via frustrated total internal reflection (FTIR). Additionally, the direct Time-of-Flight (dTOF) range measuring through time correlated single photon-counting exhibits minimal sensitivity to ambient light, facilitating the simultaneous operation of numerous sensors at the same laser wavelength [12] without significant interference.

In contrast to electrical sensing methods (such as capacitive or resistive sensing), our sensor surface does not require the integration of electrodes or dielectric multi-layers. Additionally, there is no necessity for an extensive sensor matrix to monitor a large area. Similar to other optical tactile sensor technologies, our sensing method can detect multi-touch and pressure. Our approach employs time-of-flight sensing within a wave guide and computational reconstruction of the contact area. This technique enables us to adapt our sensing method to various applications. We can alter the surface of our OptoSkin sensor to many shapes and do not depend on special or multi-layer designs. Our focus is on developing large-area sensor skins to cover various mechanical structures such as robot arms.

II. Sensing principle

We propose an original solution by integrating Time-of-Flight (ToF) sensors with wave guiding material, to enhance the performance of FTIR touch sensors. This integration aims to create the OptoSkin touch sensor platform, offering simplicity, durability, reliability, and immunity to external light conditions. This fresh approach aims to address traditional FTIR sensor limitations, particularly in achieving precise touch detection across large surfaces while maintaining speed and efficiency. This advancement holds promise in improving the versatility and practicality of touch-interface technologies. In subsequent sections, we elaborate on the underlying processes.

A. ToF sensors

Time-of-Flight (ToF) sensors measure the distance between the sensor and an object by measuring the travel time of an emitted signal. Optical ToF sensors are composed of a light-emitting component, such as a vertical cavity surface-emitting laser (VCSEL), and a photo-sensor component, such as a single-photon-counting avalanche diode (SPAD). Depending on the underlying technology, ToF sensors can be divided into direct time-of-flight (dToF) sensors which directly measure the travel time of the pulsed light and indirect time-of-flight (iToF) which emit light in a modulated pattern and calculate the shift in the measurement, computing the distance as a post-processing step (see the work of Piron et al. [13] for a more in-depth review about ToF sensors).

We are interested in dToF sensors that emit a short pulse of light with a width of σ towards the objects in the scene S, scatters back and arrives to the sensor. In these devices emitter and sensor a co-located on the same chip. Fig. 1 (a) illustrates this time of flight of a light pulse in a time-range

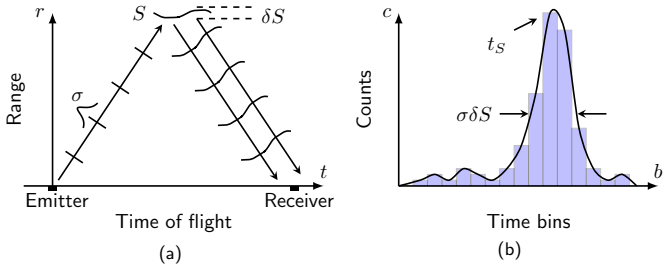

Fig. 1: A time-range diagram (a) illustrates the time-of-flight measurement process. The scene S is illuminated by a light pulse σ, the returning light is recorded and the roud-trip time t_S is measured. Using single photon-counting devices, the transient signal (b) is formed as a histogram of many single measurements. The signal has a width that is determined by the width of the instrument response (dominated by the light pulse σ and the sensor resolution) and the geometry of the observed scene δS.

diagram. As the SPAD sensor can measure the time of a single event, the measurement must be repeated to be statistically reliable. Thus, the dToF sensor outputs histograms of counted events along time, see Fig. 1 (b). This statistical measurements are processed to choose the time bin that corresponds to the measured object.

From the histogram, the ToF algorithms choose the time t_{ToF} associated with the round-trip time of the light from the sensor to the object (e.g., the time associated with the maximum value of the histogram). The distance d between the sensor and the object is proportional to t_{ToF} measured by the ToF sensor and is computed as

$$d = \frac{t_{\text{ToF}}}{2} c, \tag{1}$$

where c is the speed of light.

The distance measurement resolution Δd that we can obtain depends on the time resolution Δt_{ToF} of the ToF sensor and can be computed by applying Δt_{ToF} and Δd to Equation 1. This means that for a centimeter resolution in measured distance the ToF sensor must have picosecond time resolution. In addition, ToF sensors also have an angular range and resolution that depends on the field-of-illumination (FoI) of the emitting component, and on the field-of-view (FoV) and pixel resolution of the photo sensor component.

B. Optical wave guide

In vacuum, the speed of light is a general constant, $c_0 \approx 3 * 10^8 \frac{m}{s}$. But, in a medium light propagation depends on the optical density of the carrier medium. For instance, light travels slower in denser mediums like glass or water than in air. The index of refraction n_i of a medium i is the ratio of the speed of light in vacuum c_0 compared to the speed of light in the medium c_i ($n_i = c_0/c_i$), so a medium with higher index of refraction indicates slower light propagation.

When the light propagation path intersects with a different medium, part of the light is reflected and part of the light is transmitted to the new medium. This new medium has a

different index of refraction and the speed of light changes according to

$$c_2 = \frac{n_1}{n_2} c_1, \tag{2}$$

where n_1 and n_2 are the indices of refraction and c_1 and c_2 are the speeds of light in the origin (carrier) and new (recipient) mediums, respectively. The part of the light that enters the new medium is refracted relative to the surface orientation (normal vector), according to Snell's law

$$n_1 \sin\theta_1 = n_2 \sin\theta_2, \tag{3}$$

where θ_1 is the angle of incidence and θ_2 is the angle of refraction.

When light passes from a medium with higher index of refraction to another one with lower index of refraction, $n_1 > n_2$, then total internal reflection (TIR) might happen if the incidence angle θ_1 is greater or equal to a critical angle θ_c

$$\theta_1 \geq \theta_c = \arcsin \frac{n_2}{n_1}. \tag{4}$$

In that case, light is completely reflected back into the original medium, without refracting. At lower angles ($\theta_1 < \theta_c$), the light is subject to reflection and transmission, as mentioned above and described in the Fresnel formula [14].

TIR is the principle used by optical wave guides, such as optical fibers, for lossless or low-loss transmission of optical signals. Typically, a optical fiber is composed of a carrier material with a high index of refraction, called the core, surrounded by a low index of refraction material, called the cladding. Our wave guides will use only the carrier material with higher index of refraction then the surrounding air.

C. ToF sensors in an optical wave guide

The proposed touch sensing technology is made up of dToF sensors attached to optical wave-guiding materials. The light emitted by the dToF sensor enters the optical wave guide, is propagated inside by TIR and reaches the end of the optical wave guide. Part of the light is refracted outside the wave-guide material and part is reflected back inside the material, to be propagated in the opposite direction in the optical wave guide until reaching the ToF sensor (Fig. 2 (a)).

ToF sensor algorithms to compute object distance based on the captured histogram assume that light is propagated in an open space composed of air, but this assumption is no valid in our setup as light propagated through the wave guide medium. Further, light propagation changes direction when the light enters or exits the optical wave guide due to Snell's law (Eq.3). This effect impacts the field of illumination (FoI) and field of view (FoV) of the ToF sensor to the same extent. If we assume that the index of refraction of air $n_0 \approx 1$, the index of refraction of the wave guide n_1 and the the original FoI / FoV angle of the ToF sensor θ_0, the effective FoI / FoV angle inside the optical wave guide θ_1 is

$$\theta_1 = \arcsin\left(\frac{n_0}{n_1}\sin(\theta_0)\right). \tag{5}$$

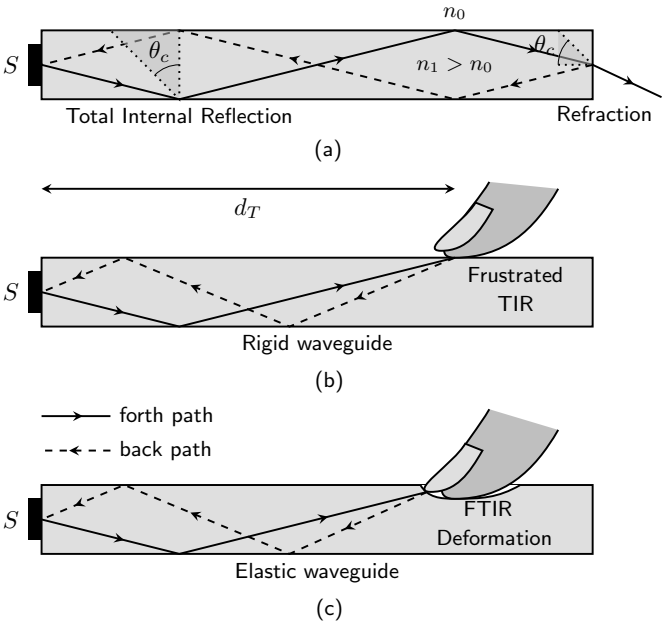

Fig. 2: Within the OptoSkin, light is propagating through the wave guide by (a) total internal reflection ($n_0 < n_1$). In the touched area, light is reflected by (b) interaction of light with environment ($n_2 \neq n_0$) through frustrated total reflection conditions e.g. scattering from skin ($n_2 \approx n_1$) and due to (c) deformation (elastic material) of the wave guide surface.

Moreover, we have to modify the computed distance from the sensor to the object from the round-trip time (Equation 1) as

$$d = \frac{t_{\text{ToF}}}{2} c_1 = \frac{t_{\text{ToF}}}{2} \frac{n_0}{n_1} c_0 \text{ with } n_1 > n_0, \tag{6}$$

taking into account the speed of light inside the optical wave guide c_1 according to Equation 2. The higher index of refraction of the wave-guide material ($n_1 > n_0$) provides an increased distance resolution Δd maintaining the time resolution of the ToF sensor Δt_{ToF}, which can be computed applying Δd and Δt_{ToF} to Equation 6.

On the other hand, the optical power P_R received by the sensor depends on the optical power emitted P_T and its propagation through the material. The optical power density is attenuated due to divergent illumination and reflection, scattering, and absorption. P_R can be calculated from the LiDAR equation, as found in many textbooks [15], [16],

$$P_R \propto \rho \frac{\eta_{\text{atm}}^2}{R^2}, \tag{7}$$

with R the detection range and $\eta_{\text{atm}}^2 = e^{-2\mu R}$ describing the the two path attenuation process (illumination and reception path) in the propagation medium, here, the atmosphere. Hence, $\mu = \mu_{\text{sc}} + \mu_{\text{abs}}$ is the atmospheric attenuation coefficient describing the absorption and scattering process.

In air, see Fig. 3 (a), the atmospheric attenuation coefficient μ is low to attain a visibility on the meter-to-kilometer scale. Here, the dominant attenuation process that limits the maximum detection range is due to the divergence of the laser source ($1/R^2$) component.

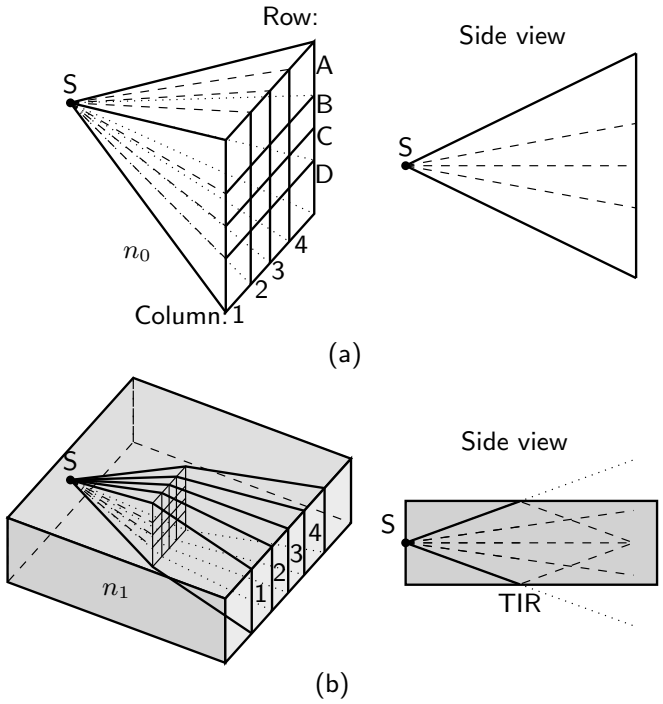

Fig. 3: Illustration of the sensor's field of view (FoV) (a) in air and (b) in an optical wave guide. Due to TIR, in (b), the signals mix along the columns of the sensor array.

Due to the TIR in our wave guide, the divergence of the light is limited in one direction; see Fig. 3 (b), so that the $1/R^2$ attenuation is not valid in our case. However, due to the strong scattering of light in the polymer material, its divergence can be neglected and the scattering described by η^2_{atm} can be identified as the dominant process.

However, since the actual behaviour of the signal strength as a function of distance is not known, we will later use reference measurements to normalize the measured signals and thus correct the dependence of the signal on the distance. In this way, we can also compensate for the material- and geometry-related inhomogenities of the wave guide.

Additionally, as demonstrated in Fig. 3 (b), it is unnecessary to employ the complete resolution of the sensor array because signal diffusion occurs along the columns due to total internal reflection (TIR). Furthermore, we specify a sector for each column in the sensor array, as every column captures photons that return from a specific angle range denoted by $\theta_i \pm \delta\theta_i$. Here, θ_i represents the mean viewing angle of the i$^{\text{th}}$ sensor sector and $\delta\theta_i$ denotes the width of the reception area. Consequently, in later discussions of outcomes, we primarily consider the time-of-flight (ToF) sensor analogous to line sensors.

D. Touch sensing

Two distinct mechanisms are utilized for touch sensing: one involves a wave guide constructed from a rigid material such as glass or resin, called the HardSkin sensor, and the other uses a wave guide made from an elastic material such as silicone rubber, referred to as the SoftSkin sensor. More information about these sensors can be found in Sect. IV. In both types of wave guides, total internal reflection (TIR) occurs when light meets an interface with a medium that has a lower refractive index (such as glass to air) and the incidence angle is larger the critical angle.

In instances where another medium comes into contact with the wave-guide interface, such as a human finger (considering that the refractive index of human skin is approximately equal to $n_{\text{human}} \approx 1.5$ [17], [18]), it can interfere with TIR and prompt light rays to refract and leave the wave guide. This phenomenon, known as Frustrated Total Internal Reflection (FTIR), has found applications in multi-touch screen sensing [3] and force sensors [19]. When the material inducing FTIR (e.g. human skin) exhibits partial diffusion, it will scatter light in various directions, allowing some of the scattered light to reenter the wave guide and travel back towards the sensor, as illustrated in Fig. 2 (b).

In our study we harness FTIR for touch detection within the wave guide, as incoming light from the ToF sensor gets reflected back at the contact point, reaching the ToF sensor at t_{touch}. Consequently, the distance to the touch location, represented by d_{touch}, can be derived utilizing Equation 6.

In addition, if the material of the wave guide is elastic, it is deformed on contact, which changes its physical shape (see illustration in Fig. 2 (c)). In that case, the angle of incidence of the light, which previously created TIR, will be greater with respect to the normal at the locally modified surface, and might cause light to refract outside the wave guide. Similarly to before, if the material of the object causing the deformation is partly diffuse, it will scatter light in all directions and reflect back light to the ToF sensor. Note that while in the HardSkin approach, only the FTIR principle due to a change of interfaces is present, in SoftSkin both a change of interfaces and a change of the shape locally at the touch point is present.

E. Reconstruction of touch location

The touch location is reconstructed from the captured histogram, where touch is detected due to the reflected light that has arrived at the sensor from FTIR. We propose to create a sensor-centered likelihood heat map of touch by projecting the captured histogram on the surface of the planar wave guide, taking into account the angular coverage of the ToF sensor that depends on the FoV and FoI.

Assuming a very thin wave guide, we consider $z \approx 0$, so we can assume that the measured distance values (d) and the sensor sections (θ, the angle of reception) represent polar coordinates $\mathcal{P}_{d,\theta} = (d, \theta)$. These values can be transformed into Cartesian coordinates $\mathcal{C}_{x,y}$ by transformation of the coordinate system:

$$\mathcal{P}_{d,\theta} \rightarrow \mathcal{C}_{x,y}: \begin{array}{rcl} x & = & d\cos(\theta) \\ y & = & d\sin(\theta) \end{array} \tag{8}$$

Let us further assume that we determine d and θ with a certain accuracy, which are denoted by the errors σ_d and σ_θ respectively. Here $\sigma_d \approx \Delta d$ is the range resolution of the sensor and $\sigma_\theta \approx \delta\theta$ is the angular width of the specific sensing section.

To transfer these errors to the Cartesian coordinates, we can use the following formulas:

$$\sigma_x = \sqrt{(\cos(\theta))^2\sigma_d^2 + (d\sin(\theta))^2\sigma_\theta^2} \quad (9)$$

$$\sigma_y = \sqrt{(\sin(\theta))^2\sigma_d^2 + (d\cos(\theta))^2\sigma_\theta^2} \quad (10)$$

We can simplify Eqs. 9 and 10 by using the small angle approximation ($\theta \to 0 : cos(\theta) = 1, sin(\theta) = 0$) to obtain the following expressions:

$$\sigma_x \approx \sigma_d \quad (11)$$

$$\sigma_y \approx d\sigma_\theta \quad (12)$$

In setups using a single sensor, the precision in pinpointing the touch location along the x- and y-axes greatly depends on the ToF sensor's characteristics. The error in accuracy along the x-axis, denoted by σ_x, is primarily determined by the sensor's range resolution. In contrast, the accuracy error along the y-axis, denoted by σ_y, is related to the sensor field of view and increases proportionally with the measured distance, later expressed as a percentage of this distance.

In fact, there are discrepancies in the optical path lengths between multiple reflection paths and direct line-of-sight. Nevertheless, these disparities are too insignificant to be registered by our sensors. Moreover, we employ comparatively narrow wave guides, thereby eliminating the necessity to modify the propagation path for multiple reflection paths. Therefore, our reconstruction algorithm o des not accounts for the curvature of the wave guide, regardless of whether it is curved or flat, and enables us to map the reconstructed data onto a 3D model.

Thus, limiting the OptoSkin sensor size, the accuracy of our approach is sufficient for human-robot interaction (HRI) applications that require precise localization of touches, such as gesture recognition and robot manipulation. By investigating configurations that involve multiple time-of-flight sensors, we expect to further refine the accuracy of touch localization.

III. Simulation

The sensing principle of OptoSkin, explained in previous section, has initially been evaluated through physically-based simulation. This allows us to demonstrate the sensing principle under perfect and controllable conditions. Later, in Sect. IV, an experimental evaluation is performed.

The general simulation setup consists on an optical wave guide and one or multiple time-of-flight sensors attached to it (Fig. 4). The wave guide materials of the simulation setup are transparent, without scattering or absorption, to test the sensing principle. We simulate the output histogram of the ToF sensor by using a modified version of the Mitsuba 3 rendering software [20] adapted for transient light transport [21], [22], being able to simulate the light's time-of-flight. The transient data obtained from these simulations is similar to real sensor data and describes the returning signatures over time. Then we apply the touch reconstruction algorithm described in Section II-E and obtain a likelihood heat map of touch (Fig. 5 (a)).

Simulations facilitate the investigation of OptoSkin configurations under various conditions, such as changes in the ToF characteristics (time resolution, FoV, and FoI), arrangements of ToF sensors, wave-guide geometries, and optical traits (for example, scattering, absorption). For example, in Fig. 5 (b), two simultaneous touches are detected at different areas of the surface using an arrangement of six ToF sensors strategically placed (Fig. 4 (b)). Additionally, the simulation can include a wave guide made of a elastic material subjected to varying pressures, examining how changes in the wave guide's shape influence touch detection. Fig. 6 shows that the touch signal increases with greater deformation caused by increased pressure.

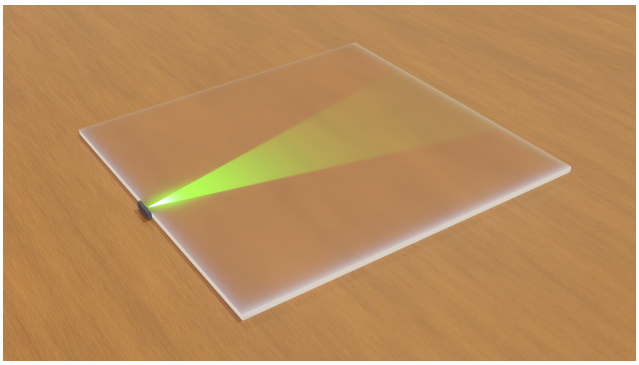

(a) One sensor

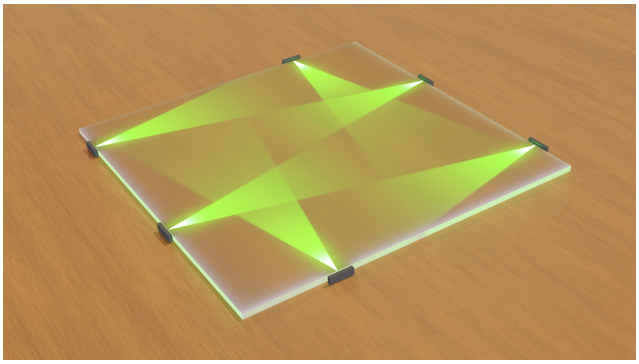

(b) Multiple sensors

Fig. 4: Virtual representation of the setup used to simulate the OptoSkin sensing principle using different configurations of ToF sensors attached to the wave guide: (a) single sensor and (b) distribution of six sensors.

Fig. 5: Touch reconstruction on a HardSkin sensor: (a) one touch detected by a single ToF sensor and (b) dual touches detected using six ToF sensors.

IV. Experimental investigation

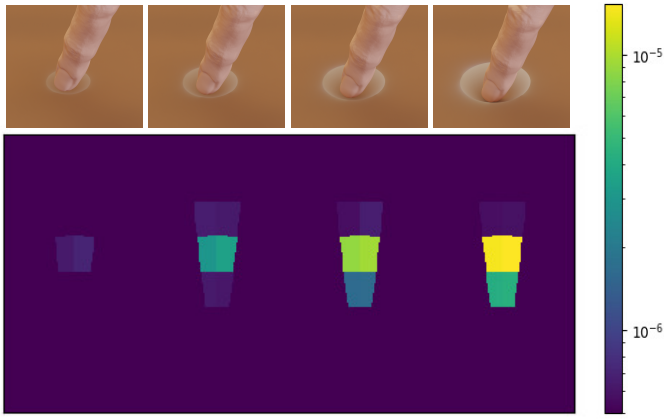

Fig. 6: Reconstruction of four touch events with increasing pressures in a SoftSkin wave guide.

TABLE I: Evaluation of some wave-guide material candidates: photo-polymers for 3D printing, silicone rubber and PMMA.

Name	n	R_{dif} [%]	T [%]	μ_A $[cm^{-1}]$	μ_S $[cm^{-1}]$	Comment
3D printed rigid photo-polymer resin						
Crystal Clear	1.483	6.6	88.6	0.1	0.2	transparent, clear
Tech Clear	1.537	7.4	82.1	0.14	0.8	transparent, blue
Clear Impact	1.523	7	82.5	0.15	1.1	transparent, yellow
Soft silicone rubber						
TFC4190-T19	1.400	4.9	84.4	0.14	0.6	transparent, clear
Crystalflex	1.398	1.9	88.2	0.06	0.1	transparent, clear
Flexible PMMA wave guide						
1216.1013	1.498	tbd	93.3	0	0	transparent, clear

A. Wave-guide material selection

We investigated the optical and mechanical properties of different wave-guide material candidates. All in all, we characterized a soft silicone rubber, 3D printed rigid photo polymer resins and a flexible poly-methyl-methacrylate (PMMA) fibers.

When light encounters inhomogenities in the material, it can be scattered in various directions, leading to a reduction in the intensity of the transmitted light. Thus, the scattering coefficient μ_S is a measure of the scattering ability of inhomogenities in the material which scatter optical power out of a light beam. In addition, the absorption coefficient μ_A quantifies the absorption of light by the medium itself. These coefficients are fundamental in fields such as optics, atmospheric science, and materials science, where understanding light interactions is essential for various applications.

We measured the transmittance T, reflectance R and diffuse reflectance R_{dif} in a spectral range of $175\,\text{nm}$ to $3300\,\text{nm}$ using a universal measurement spectrometer (Cary 7000, Agilent, Santa Clara, United States). The scattering coefficient μ_S was obtained according to guidelines of F. Foschum et al [23], [24].

Additionally, the Metricon Model 2010/M Prism Coupler [25] was utilized for atypical samples like 3D printed and flexible materials to determine the refractive index n at specific angles across three wavelengths ($1064\,\text{nm}$, $632.8\,\text{nm}$ and $532\,\text{nm}$). In these instances, the refractive index at $940\,\text{nm}$ was approximated by fitting the experimental data to Cauchy's equation $n = A + \frac{B}{\lambda^2} + \frac{C}{\lambda^4}$ [14], [26]. Additionally, the refractive index for silicone samples was measured using a spectral ellipsometer (RC2 – XI, J.A.Woollam, United States).

TABLE II: Evaluation of some Lidar on integrated circuit chips with histogramming function.

Name	Sensor (Array)	Laser (λ)	FOV	Time bin width
AMS TMF8828	SPAD (8x8)	VCSEL (940nm)	$41\,^\circ \times 52\,^\circ$ $0.7\,\text{rad} \times 0.9\,\text{rad}$	$100\,\text{ps/bin}$
STMicro. VL53L8	SPAD (8x8)	VCSEL (940nm)	$45\,^\circ \times 45\,^\circ$ $0.8\,\text{rad} \times 0.8\,\text{rad}$	$250\,\text{ps/bin}$

In Tab. I, the optical properties of selected wave-guide materials are summarized. We present the measured refractive index n, the diffuse reflectance R_{dif}, the transmittance T, the absorption coefficient μ_A, and scattering coefficient μ_S are given at $940\,\text{nm}$. This wavelength corresponds to the typical emitter wavelength of time-of-flight sensors. The 3D printed materials (rigid photopolymers) have slightly higher refractive index n respect to silicone rubber due to higher density. Further, the 3D printed materials have also larger diffuse reflectance R_{dif} due to higher surface roughness respect to silicone rubber. All evaluated materials show similar transmittance T in the rage from $82\,\%$ to $88\,\%$ due to low light scattering. The highest transmittance T and no light scattering was found for the PMMA flexible wave guide, providing ideal light guiding conditions.

Based on our examinations, we determined that using the PMMA Fiber (Mentor, Germany), the Tech Clear resin (Moiin, Germany) for 3D printing, and the silicone rubbers (TFC, Germany and Samson Kamnik, Slovenia) for cast polymerization would be suitable for fabricating various OptoSkin sensors, namely the SoftSkin and HardSkin prototypes.

B. Sensor selection

At the time of the study, there were various commercially available integrated laser ranging sensors, known as LIDAR on integrated circuits (LoIC). A non-exhaustive list of these sensors can be found in Tab. II. These sensors are engineered to detect the proximity of surfaces by using direct time-of-flight laser ranging technique, as described in Sec. II-A. The sensors typically include a laser source for emitting light pulses and a highly sensitive detector to capture the returning echo. Generally, the sensor is built around a single photon counting avalanche diode (SPAD) array, while the light source is a vertical-cavity surface-emitting laser (VCSEL), with both components integrated onto a single silicon chip.

Generally, the laser emission is minimal, and the laser sources are classified as Laser Class 1 [27]. This ensures no damage to human eyes and eliminates the need for protective measures for the user (skin or eyes). Additionally, we did not detect any thermal effects from the waveguide's absorption of optical power.

Given that these sensors can detect individual photon events, they automatically execute thousands of separate measurements and provide the most likely range value. Moreover, certain models, such as the VL53L8 (STMicroelectronics, Switzerland) and TMF8828 (AMS-OSRAM, Austria), offer a

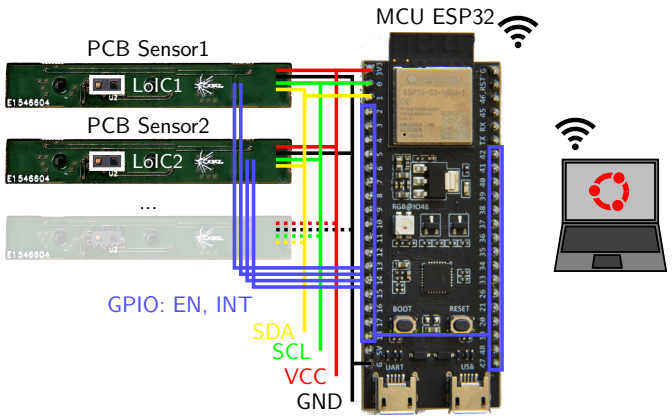

Fig. 7: Multiple laser ranging sensor modules (LoICs) can be controlled and read out by a microprocessor controller unit (MCU) through separate inter-integrated circuit (I^2C) communication lines.

histogram function that returns the signal's temporal profile. This feature is particularly beneficial when measuring in scattering environments, enabling users to apply custom advanced analysis algorithms. Both sensors possess sub-nanosecond time resolution; however, due to its high temporal resolution of $100\,\mathrm{ps/bin}$, we opted to utilize the TMF8828 sensor for subsequent experimental investigations.

C. Experimental setups

Our setups consist of two main components, the electronics and the wave guides, and are described in detail below.

1) Electronic boards: The electronic layout of our setups is sketched in Fig. 7. For each setup, we use a single micro controller unit (MCU) (e.g., ESP32, Espressif Systems, CN) to control and read out several sensors using the I2C (Inter-Integrated Circuit) serial controller bus. The recorded data is processed on the MCU and transmitted to a main computer via a wireless network.

We realized small printed circuit boards (PCB) equipped with a single sensor (LoIC) and driver electronics to install different sensors at the wave guides. In our setups, we use the TMF8828 proximity sensor which is capable to return by default histograms of the recorded signals. Each daughter board is connected to the MCU by joint power (VCC), ground (GND), I2C clock (SCL) and data (SDA) line. Further each sensor has two individual connections: the enable bus (EN) is used to switch the individual sensors on and off, and the interrupt (INT) is used to receive messages from the sensor when new data is available.

2) Wave guides: We have realized four versions of the OptoSkin sensor, as depicted in Fig. 8, using different material (see Tab. I) and processing methods. The parameters of the different setups are described in the following and are summarized in Tab. III. In the given configurations, we expect to localize the touch point within the sensor field of view with a precision of about $\sigma_x \approx \frac{\Delta t_{\mathrm{ToF}}}{2}\frac{c}{n_1} = 1\,\mathrm{cm}$ and $\sigma_y \approx 0.1x$.

A first sensor, Fig. 8 (a), consists of a one-dimensional rod made of flexible PMMA with a length of $115\,\mathrm{mm}$ and a diameter of $3\,\mathrm{mm}$. This sensor can only sense the range of the touch and was used for first investigation of touch sensing and to demonstrate the fundamental sensing principles.

TABLE III: Realized OptoSkin demonstrators.

Name	Material	Shape	Dimensions	σ_x	σ_y
Rod	PMMA	1D rod	l = 115 mm, d = 3 mm	1 cm	11.1 %
HardSkin	resin	2D curved	180 °, R = 60 mm, d = 5 mm	0.98 cm	10.8 %
SoftSkin 1	silicone	2D flat	30 cm × 30 cm, d = 5 mm	1.07 cm	11.9 %
SoftSkin 2	silicone	2D flat	30 cm × 30 cm, d = 10 mm	1.07 cm	11.9 %

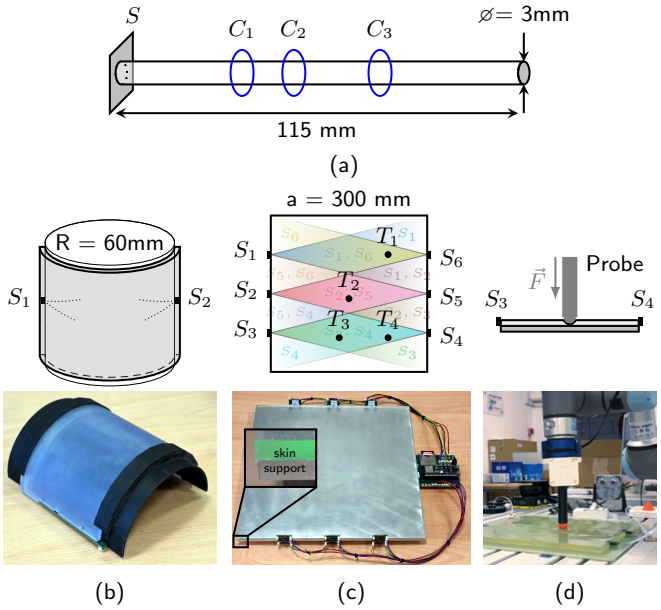

Fig. 8: Sketches and images of our technology demonstrators with (a) a flexible PMMA rod, (b) a 3D printed rigid optical wave guide (HardSkin) and two SoftSkin models, (c) and (d), based on an elastic silicone rubber.

A second sensor, Fig. 8 (b), has a rigid quasi-two-dimensional wave guide made of hard resin (HardSkin). This wave guide was 3D printed in a photopolymerization process by layer-by-layer illumination with ultraviolet light (printer: Saturn 2, Elegoo, CN) using Tech Clear resin. We printed wave guides with various shapes and realized, among others, a curved wave guide with the shape of a semi-cylindrical hull with a radius of $R = 60\,\mathrm{mm}$ and a curvature angle of $180\,°$. The wave guide has a thickness of $5\,\mathrm{mm}$, a height of $10\,\mathrm{cm}$, and a curvature length of about $18.85\,\mathrm{cm}$. We have mounted two sensors opposite each other, aligned tangentially to the curvature of the wave guide. In this configuration, the TIR bends the field of view along this curvature. The sensor was set up to cover a cylindrical support structure such as a robot arm (e.g. UR10).

In addition, we have set up two SoftSkin sensors consisting of wave guides made of elastic silicone rubber with the consistency of soft skin. The wave guides were created in a cast polymerization process by pouring the silicone onto a

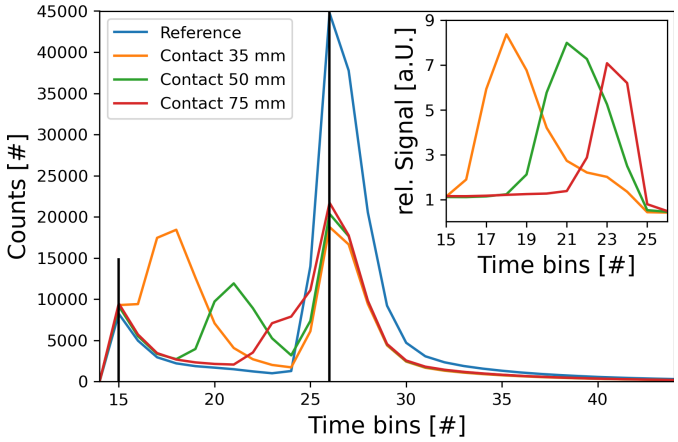

Fig. 9: Signatures of a finger touching the Rod sensor at different contact points at distances C1 = 35 mm (orange), C2 = 50 mm (green) and C3 = 75 mm (red). The data is compared to the signature of the Rod sensor without contact (blue). The inset shows the relative signal of the three touch events.

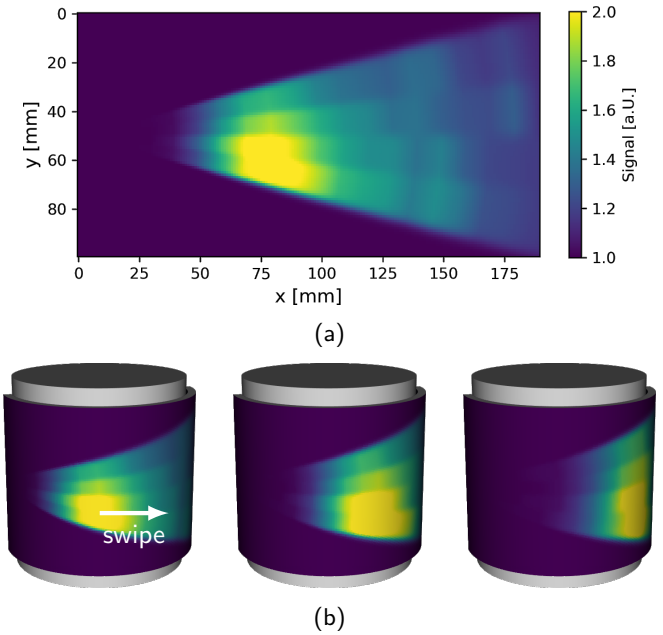

Fig. 10: Experimental results for the HardSkin demonstrator as (a) a single 2D color map showing a hand touching the sensor surface and (b) a time series of color maps projected onto a 3D model showing a swiping gesture.

support structure (e.g. aluminum plate) during polymerization. The silicone wave guides had to dry (heal) for several hours before the sensors could be installed.

As shown in Fig. 8 (c), the first SoftSkin sensor (SoftSkin 1) was made of TFC4190 silicon rubber with a stiffness of Shore 00-80 and has a dimension of $30\,\mathrm{cm} \times 30\,\mathrm{cm}$ with a thickness of $d = 5\,\mathrm{mm}$. Six sensors have been installed, arranged in sets of three facing each other. In this configuration, the sensors' fields of view cover about $87.5\,\%$ of the SoftSkin surface ($25\,\%$ covered by a single sensor and $62.5\,\%$ covered with two sensors). We set up this sensor to demonstrate the application of multiple ToF sensors and to localize touch events.

The second SoftSkin sensor (SoftSkin 2), shown in Fig. 8 (d), has the dimensions of $34\,\mathrm{cm} \times 30\,\mathrm{cm}$ with a thickness of $d = 10\,\mathrm{mm}$. Along the two shorter sides, 4 ToF sensors are installed in a configuration that ensures maximal sensor field-of-view coverage and minimal overlap. Mechanical adapters, into which up to four removable ToF sensors may be inserted, are embedded into the silicone. Additionally, we detached the silicone rubber from the casting support structure, allowing the SoftSkin to be mounted on various supports and utilized in multiple configurations. This formulation allows the prototype to be deployed either in a flat configuration or wrapped around cylindrical objects, such as robot arm segments, while ensuring optimal contact between the ToF sensors and the silicone rubber.

D. Experimental Results

We used all four experimental setups to examine the time-of-flight propagation in an optical wave guide with different focus depending on the specific sensor setup.

1) Rod wave guide: The 1D Rod wave guide was used to investigate the underlying principle of detecting signatures from interaction of the applied laser pulse with human tissue that are fingers touching or gripping the wave guide. The interaction process relies on frustrated total internal reflection (FTIR) that is light partly reflected within the wave guide and partly transmitted into the human tissue. Within the tissue the light is diffused and scattered back into the wave guide. During this process, part of the laser light is scattered back towards the TOF sensor detecting the transient signal.

In Fig. 9, we show transient signals recorded without (blue) and with touching the Rod wave guide at three different positions (orange, green and red). In the reference signal (blue, without touch) we can observe to peaks, at time bin 15 and 26, which can be identified as reflections of the laser pulse at the wave guide's entrance and exit facet. These signatures are the background signal which specific for the applied wave guide and they are visible in all measurements.

Touching the wave guide, gives additional responses mixing with the background signal. Clearly, the signal can be distinguished from reference for three different contact distances ($d \approx 35\,\mathrm{mm},\ 50\,\mathrm{mm}$ and $75\,\mathrm{mm}$). For better visibility, the relative signals are shown in the inset for time bins of interest ($b \in [15, 26]$) . Further, in our investigations, we could show that this kind of touch sensing works with a bending curvature of the 1D wave guide up to diameter of $80\,\mathrm{mm}$ without affecting the signal and the contact point detection. This curvature is sufficient to cover mechanical structures such as robotic arms (e.g. UR10).

2) HardSkin: As mentioned above, the HardSkin sensor has quasi 2D wave guide with a semi-cylindrical curvature. Therefore, the recorded signatures can be displayed in a 2D color map allowing us to localize the touch point on the skin surface. In the experiments we used only one of the two mounted ToF sensors.

In Fig. 10 (a) we show an exemplary result of a hand

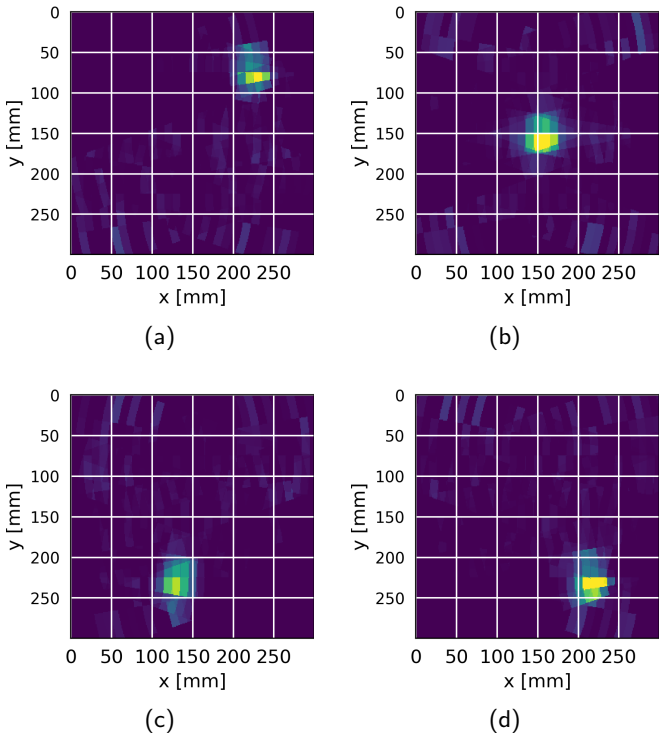

Fig. 11: Results for the SoftSkin 1 sensor to localize the touch point on the SkinSurface. We tested four different positions.

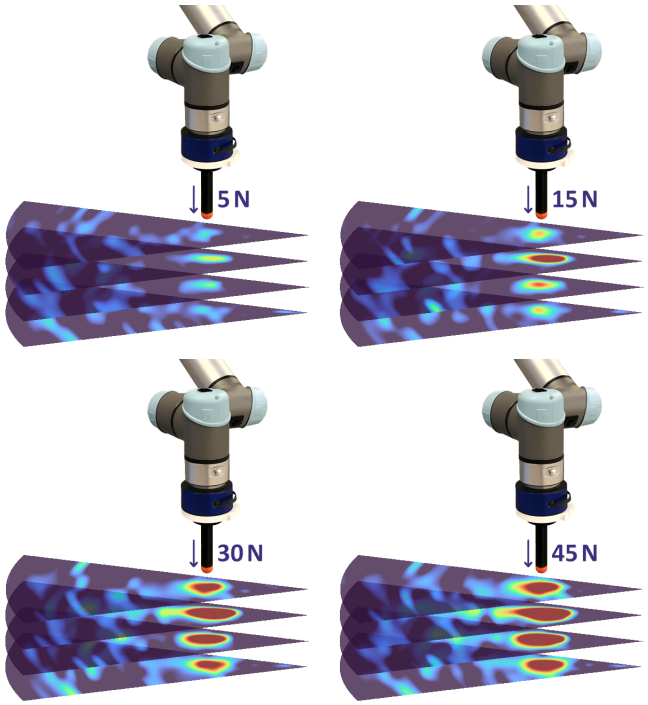

Fig. 12: Simultaneous localization and pressure sensing with the SoftSkin sensor. Diagrams show the sensor response as different contact force magnitudes, ((a) 5 N, (b) 15 N, (c) 30 N and (d) 45 N), are being applied onto the skin with a probe.

touching the HardSkin sensor. The 2D heat map showing the relative location of the touch point as position along the surface range or tangential position (x) and the surface height (y). We can identify a single contact area at $x = 60\,\mathrm{mm}$ and $y = 75\,\mathrm{mm}$.

In addition, the 2D heat maps can be used to locate the touch point in 3D space by projection of the maps onto a spatial model. In Fig. 10 (b), we project heat maps onto a cylindrical surface model. The figure illustrates a time series of results showing the signature of a hand swiping over the sensor surface. Here, we can observe the movement of the contact point on the projection model and could analyze the gesture to control the robot. The 3D model gives the exact position of the touch point in robot model.

3) SoftSkin 1: The SoftSkin 1 sensor is a two-dimensional skin equipped with six ToF sensors. Each sensor was used to monitor a certain region of the sensor skin, and most of the sensor surface was covered by at least one sensor. Therefore, the SoftSkin 1 sensor was set up to investigate the localization of touch points in a multi-sensor configuration.

In Fig. 11 we show a series of color maps showing the signature of a probe touching the sensor at different locations, T_1 to T_4. In these cases, (a)-(d), the touch event was detected only by the sensors dedicated for that specific skin surface region. The sensors did not return a signature if the touch event took place outside their field of view. Therefore, we could proof the reliability of the sensing process and the robustness against false detection events. Further, by combining touch sensing from different ToF sensor with different aspect angles, it is possible to enhance the precision of the localization to $\sigma_x < 1\,\mathrm{cm}$ and $\sigma_y < 1.5\,\mathrm{cm}$.

4) SoftSkin 2: In addition to point-of-contact localization, we have investigated whether SoftSkin can be used to estimate the contact force applied to its surface. The underlying principle revolves around the use of frustration total internal reflection (FTIR) to interpret sensor signals, which are influenced by both the contact surface area and the depth of surface deformation. Consequently, as the applied force on the SoftSkin increases, so does the deformation of the silicone rubber, resulting in corresponding changes in the sensor signal values.

To achieve accurate and consistent measurement results, a robotic arm (UR5e, Universal Robots, DK) was utilized, equipped with a blunt end effector and a wrist force and torque sensor (JR3, Woodland, USA). This setup enables the simultaneous application and measurement of various force magnitudes at specific coordinates on the surface of the SoftSkin prototype.

Fig. 12 illustrates the sensor responses, grouped in four horizontal layers, when subjecting the SoftSkin to different force magnitudes: (a) 5 N, (b) 15 N, (c) 30 N, and (d) 45 N. Each horizontal layer represents the responses in four adjacent detection zones that measure in the same horizontal plane (see Fig. 3; rows A,B,C,D).

With an applied force of 5 N (a), the touch signature begins to stand out clearly from the background noise. When the force increases, as shown in (b), (c) and (d), these signatures become increasingly pronounced and clear. Sensor response amplitudes vary layer by layer. As the pressure applied to the

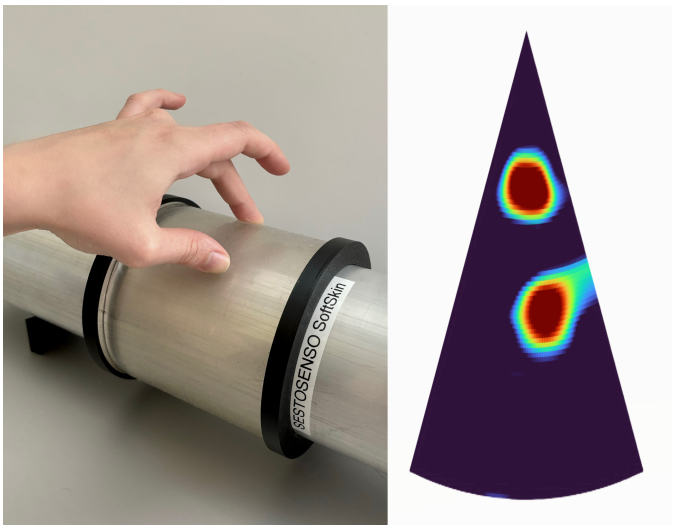

Fig. 13: Usage of the SoftSkin sensor on a cylindrical structure (left) to demonstrate the performance of a single ToF sensor in an application-related scenario. The heat map (right) shows the interpolated sensor response in a situation with multiple contact points and simultaneous localization.

silicon rubber increases, we observe a corresponding increase in both the signal amplitude and the detection area from the time-of-flight sensor. However, the mean position of the detection remains unchanged. These initial results demonstrate that SoftSkin sensors can also be used to assess the pressure or force applied.

During the experiments, a systematic increase in contact forces was applied in increments of 3 N (with a penetration depth of corresponding 1 mm). We found that contacts applying a force of 3 N were successfully detected by the ToF sensor within a distance of 20 cm. However, contacts exerting higher force levels of 6 N could be detected over the entire SoftSkin prototype's surface. Based on this data, the contact detection threshold is estimated at around 5 N.

In Fig. 13, the SoftSkin was installed on a cylindrical structure to illustrate its application, for example, on a robotic arm like the UR10 (Universal Robots, DK). The heat map displays a scenario of multi-touch feedback. In this instance, the operator touches the sensor skin with two fingers at separate locations simultaneously. Due to the TIR light propagation, the light is only partially reflected at the initial contact point, allowing it to continue and detect subsequent contact points as well.

Further, during non-contact situations, it has been observed that OptoSkin sensor's baseline responses exhibit variances between curved and straight geometries. However, upon implementation of our calibration procedure, the baseline offsets is eliminated from the output signal. According to our preliminary assessment, the pressure measurement, which depends on the deformation of the SoftSkin surface, did not reveal any significant discrepancies or deviations in the measurements during this study.

V. Conclusion

We have demonstrated the fundamental principle of our proposed OptoSkin touch sensor through both simulation and experiment. We have developed four different prototypes, each with unique features and capabilities, to showcase the versatility and applicability of our approach. Our results indicate that the proposed sensor is capable of localizing touch events on 1D (Rod) and 2D surfaces (HardSkin, SoftSkin1 and SoftSkin2), and projecting them onto 2D and 3D structures. This opens up new possibilities for developing sensors that can detect and respond accurately to touch inputs in various applications.

One of the key advantages of our proposed sensor is its electrode-free surface, which simplifies sensor design and integration. Conventional electrical (resistive or capacitive) touch sensors rely on complex electrode configurations, which can make them difficult and expensive to manufacture and integrate into devices. In contrast, our sensor uses a simple and elegant approach that eliminates the need for electrodes altogether. This not only makes the sensor easier to fabricate but also allows it to conform to irregular surfaces, expanding its potential use cases.

Another advantage of our proposed sensor is its co-located light source and detector. By integrating these two components into a single unit, we can streamline electronics, reduce energy consumption, and improve overall compactness. This is in contrast to traditional touch sensors, which often require separate light sources and detectors, adding to the complexity and cost of the system.

In addition to demonstrating and characterizing pressure/force detection for the first time, our results also highlight the potential of the proposed sensor as a viable alternative to traditional touch sensors. The advantages discussed above make it an attractive option for a wide range of applications, from consumer electronics to medical devices, where accurate and reliable touch sensing is critical.

During our experiments, we have not observed any permanent deformation of our SoftSkin sensors. However, subjecting the SoftSkin surface to excessive tangential forces can lead to damage. Consequently, extra precautions are recommended for such use cases. Our future developments will involve researching sophisticated structures that integrate a protective layer to increase robustness of the sensor. Notwithstanding, we postulate that, in typical applications, a strong and inflexible surface (HardSkin) will be adequate for detecting contact, with pressure being deducible from the data obtained through the robot's force and torque sensors. From our point of view, the SoftSkin sensor is more suitable for handling fragile and deformable objects, for example.

In the literature, we find various other optical sensors that exhibit two-dimensional tactile sensitivity. Among others, visual methods are used to detect FTIR [1]–[4], [7] or the deformation of a membrane [28], [29], [32]–[35] or the imprint of an elastomer layer [30], [36]–[39]. Other methods use the detection of free beams using a large number of transmitters and receivers (many-to-many) [31]. In Tab. IV we compare various performance characteristics of our OptoSkin sensor with a selection of other optical sensing methods.

TABLE IV: Summary of OptoSkin performance and comparison with different optical touch sensor technologies.

Sensor	Description	Sensing area [mm^2]	Thickness	Geometric constraints	Amount of data	Sensory capabilities	
						Touch	Pressure
Time-of-flight sensing of FTIR							
OptoSkin (ours)	Back scattering in wave guide	300×300	Thin	Flat or curved wave guides	$4\times$ 128 byte, 15 Hz (histograms)	Multi, 1 cm	3 N
Vision-based sensing of FTIR							
[7]	Re-propagated multiple reflection path	100×100	Medium	Mirror surfaces	4208 pxl$\times$3120 pxl, 30 Hz (images)	2.3 mm	—
[1]	Imaging of perpendicular scattering	240×240	d_{im}	Planar surface, multi-layer	832 pxl $\times$ 832 pxl, 30 Hz (images)	Multi, 1 mm	0.1 N
Visiflex [4]	Convex multi-layer wave guide	Diam. 30	d_{im}	Specific convex hull	640 pxl $\times$ 480 pxl, 90 Hz (images)	1 mm	0.3 N
Vision-based sensing of surface deformation							
FingerVision [28]	Marker displacement on planar membrane	31×40	d_{im}	Planar membrane	320 pxl $\times$ 240 pxl, 63 Hz (images)	Multi, 1 mm	1 N
TacTip [29]	Marker displacement on convex membrane	Diam. 30-40	d_{im}	Specific convex hull	640 pxl $\times$ 480 pxl, 90 Hz (images)	2 mm	—
GelSight [30]	Deformation of a side-lit elastic layer	Diam. 25	d_{im}	Specific planar multi-layer	320 pxl $\times$ 240 pxl, 30 Hz (images)	0.1 mm	—
Free-beam							
ZeroTouch [31]	Many-to-many free-beam detection	660×1120	Thin	Free space, planar surface	32 emitters, 512 receivers	Multi	—

We note that vision-based techniques employ a camera to capture visuals of the sensing area and utilize advanced computer-vision algorithms to interpret these images. Owing to the vastness of the imaging sensor matrix (ranging from hundreds of thousands to millions of pixels), they typically attain a high spatial resolution in the millimeter domain and some exhibit a high sensitivity to pressure ($<< 1\,\mathrm{N}$), both of which surpass the capabilities of the OptoSkin. Conversely, the size and frame rate of these images produce a large amount of data that necessitates processing (reading, storage, and analysis). This demands substantial computing power. In contrast, OptoSkin produces minimal data, which can be processed locally on an MCU or in a distributed sensor network [12].

Additionally, vision-based sensors are confined to imaging within a direct line of sight. A crucial design variable is therefore the imaging distance d_{im}, which makes the structures quite bulky. In general, the sensing area is limited to a certain surface. Moreover, free-beam sensors necessitate a flat surface. Conversely, OptoSkin enables the customization of the sensor surface to match the application geometry and permits the coverage of larger areas without the need for extra time-of-flight sensors.

Considering the described performance and attributes, other optical surface sensors are designed for specific uses, such as robotic grippers or touch screen displays (touch pads). On the other hand, our approach involves creating a tactile sensor skin that can be attached to various robot surfaces and conformed to the robot's shape. This facilitates environmental sensing, allowing the robot to maneuver even in complex and dynamic settings or to promote secure human-robot interaction (HRI).

In conclusion, this research has presented a novel approach to touch sensing that offers several advantages over traditional methods. Through simulation and experimentation, we have shown the fundamental principle behind our proposed sensor, realized four different prototypes, and demonstrated its ability to localize touch events on 1D and 2D surfaces and project them onto 2D and 3D structures. We believe that this research represents an important step forward in the development of next-generation touch sensors that are simpler, more versatile, and more cost-effective than current technologies.

ACKNOWLEDGMENT

This work was supported by the European Commission's HORIZON EUROPE Research and Innovation Actions under GA number 101070310.

Furthermore, Institute of Solid State Physics, University of Latvia, is a Horizon 2020 Teaming Phase 2 project beneficiary under grant agreement No. 739508 (CAMART2), funded by the European Union.

The authors would like to thank the participating institutes for their technical and administrative support of this work.

REFERENCES

[1] S. S. Desai, A. M. Eckert-Erdheim, and A. M. Hoover, "A large-area tactile force sensor for measuring ground reaction forces from small legged robots," in *2013 IEEE/RSJ International Conference on Intelligent Robots and Systems*. IEEE, 2013, pp. 4753–4758.

[2] A. K. B. Mahmood, S. Sulaiman *et al.*, "Design and implementation of multi-touch system using ftir technique for optimization of finger touch detection," in *2010 International Symposium on Information Technology*, vol. 1. IEEE, 2010, pp. 1–7.

[3] J. Y. Han, "Low-cost multi-touch sensing through frustrated total internal reflection," in *UIST 2005*, ser. UIST '05. New York, NY, USA: Association for Computing Machinery, 2005, p. 115–118. [Online]. Available: https://doi.org/10.1145/1095034.1095054

[4] A. J. Fernandez, H. Weng, P. B. Umbanhowar, and K. M. Lynch, "Visiflex: A low-cost compliant tactile fingertip for force, torque, and contact sensing," *IEEE Robotics and Automation Letters*, vol. 6, no. 2, pp. 3009–3016, 2021.

[5] S. Hodges, S. Izadi, A. Butler, A. Rrustemi, and B. Buxton, "Thinsight: versatile multi-touch sensing for thin form-factor displays," in *Proceedings of the 20th annual ACM symposium on User interface software and technology*, 2007, pp. 259–268.

[6] R. Hofer, D. Naeff, and A. Kunz, "Flatir: Ftir multi-touch detection on a discrete distributed sensor array," in *Proceedings of the 3rd International Conference on Tangible and Embedded Interaction*, 2009, pp. 317–322.

[7] R. Wattanaparinton and K. Takemura, "Vision-based tactile sensing using multiple contact images generated by re-propagated frustrated total internal reflections," in *2022 IEEE International Conference on Systems, Man, and Cybernetics (SMC)*. IEEE, 2022, pp. 962–967.

[8] P. Piacenza, W. Dang, E. Hannigan, J. Espinal, I. Hussain, I. Kymissis, and M. Ciocarlie, "Accurate contact localization and indentation depth prediction with an optics-based tactile sensor," in *2017 IEEE International Conference on Robotics and Automation (ICRA)*. IEEE, 2017, pp. 959–965.
[9] B. Jarrahi and J. Wanek, "Design of an fmri-compatible optical touch stripe based on frustrated total internal reflection," in *2014 36th Annual International Conference of the IEEE Engineering in Medicine and Biology Society*. IEEE, 2014, pp. 4952–4955.
[10] J. Hirano and D. Garmire, "Force transducer through total internal reflection and frustrated total internal reflection for a three-axis anemometer," *IEEE Sensors Journal*, vol. 15, no. 7, pp. 3827–3834, 2014.
[11] J.-T. Lin, C. A. Newquist, and C. K. Harnett, "Multitouch pressure sensing with soft optical time-of-flight sensors," *IEEE transactions on instrumentation and measurement*, vol. 71, pp. 1–8, 2022.
[12] F. Giovinazzo, F. Grella, M. Sartore, M. Adami, R. Galletti, and G. Cannata, "From CySkin to ProxySKIN: Design, implementation and testing of a multi-modal robotic skin for human–robot interaction," *Sensors*, vol. 24, no. 4, p. 1334, 2024.
[13] F. Piron, D. Morrison, M. R. Yuce, and J.-M. Redouté, "A review of single-photon avalanche diode time-of-flight imaging sensor arrays," *IEEE Sensors Journal*, vol. 21, no. 11, pp. 12 654–12 666, 2021.
[14] M. Born and E. Wolf, *Principles of optics: electromagnetic theory of propagation, interference and diffraction of light*. Elsevier, 2013.
[15] P. F. McManamon, *Field Guide to lidar*. SPIE Press, 2015, vol. FG36.
[16] U. Wandinger, *Introduction to Lidar*. Springer-Verlag, 2005, p. 1–18.
[17] M. Van Gemert, S. Jacques, H. Sterenborg, and W. Star, "Skin optics," *IEEE Transactions on Biomedical Engineering*, vol. 36, no. 12, pp. 1146–1154, 1989.
[18] T. Kono and J. Yamada, "In vivo measurement of optical properties of human skin for 450–800 nm and 950–1600 nm wavelengths," *International Journal of Thermophysics*, vol. 40, pp. 1–14, 2019.
[19] A. Lavatelli, A. Zanoni, E. Zappa, and A. Cigada, "On the design of force sensors based on frustrated total internal reflection," *IEEE Transactions on Instrumentation and Measurement*, vol. 68, no. 10, pp. 4065–4074, 2019.
[20] W. Jakob, S. Speierer, N. Roussel, M. Nimier-David, D. Vicini, T. Zeltner, B. Nicolet, M. Crespo, V. Leroy, and Z. Zhang, "Mitsuba 3 renderer," 2022, https://mitsuba-renderer.org.
[21] A. Jarabo, J. Marco, A. Muñoz, R. Buisan, W. Jarosz, and D. Gutierrez, "A framework for transient rendering," *ACM Transactions on Graphics (SIGGRAPH Asia 2014)*, vol. 33, no. 6, 2014.
[22] D. Royo, J. García, A. Muñoz, and A. Jarabo, "Non-line-of-sight transient rendering," *Computers & Graphics*, vol. 107, pp. 84–92, 2022. [Online]. Available: https://www.sciencedirect.com/science/article/pii/S0097849322001200
[23] F. Foschum, F. Bergmann, and A. Kienle, "Precise determination of the optical properties of turbid media using an optimized integrating sphere and advanced monte carlo simulations. part 1: Theory," *Applied Optics*, vol. 59, no. 10, pp. 3203–3215, 2020.
[24] F. Bergmann, F. Foschum, R. Zuber, and A. Kienle, "Precise determination of the optical properties of turbid media using an optimized integrating sphere and advanced monte carlo simulations. part 2: experiments," *Applied Optics*, vol. 59, no. 10, pp. 3216–3226, 2020.
[25] Metricon, "MODEL 2010/ M OVERVIEW," https://www.metricon.com/model-2010-m-overview, [Accessed 24-04-2024].
[26] L. Cauchy, "Sur la dispersion de la lumiere," *bull. des. sc. maht.*, vol. 14, p. 9, 1830.
[27] AMS-OSRAM, "DS000693 TMF8820/21/28 Multizone Time-of-Flight Sensor," https://look.ams-osram.com/m/52236c476132a095/original/TMF8820-21-28-Multizone-Time-of-Flight-Sensor.pdf, 2023, [Accessed 24-04-2024].
[28] A. Yamaguchi and C. G. Atkeson, "Implementing tactile behaviors using fingervision," in *2017 IEEE-RAS 17th International Conference on Humanoid Robotics (Humanoids)*. IEEE, 2017, pp. 241–248.
[29] B. Ward-Cherrier, N. Pestell, L. Cramphorn, B. Winstone, M. E. Giannaccini, J. Rossiter, and N. F. Lepora, "The tactip family: Soft optical tactile sensors with 3d-printed biomimetic morphologies," *Soft robotics*, vol. 5, no. 2, pp. 216–227, 2018.
[30] R. Li, R. Platt, W. Yuan, A. Ten Pas, N. Roscup, M. A. Srinivasan, and E. Adelson, "Localization and manipulation of small parts using gelsight tactile sensing," in *2014 IEEE/RSJ International Conference on Intelligent Robots and Systems*. IEEE, 2014, pp. 3988–3993.
[31] J. Moeller and A. Kerne, "Zerotouch: an optical multi-touch and free-air interaction architecture," in *Proceedings of the SIGCHI Conference on Human Factors in Computing Systems*, 2012, pp. 2165–2174.
[32] K. He, X. Shi, D. Yu, and X. Guo, "Vision-based high-resolution tactile sensor by using visual light ring," *IEEE Sensors Letters*, vol. 6, no. 4, pp. 1–4, 2022.
[33] Y. Zhang, Z. Kan, Y. Yang, Y. A. Tse, and M. Y. Wang, "Effective estimation of contact force and torque for vision-based tactile sensors with helmholtz–hodge decomposition," *IEEE Robotics and Automation Letters*, vol. 4, no. 4, pp. 4094–4101, 2019.
[34] C. Trueeb, C. Sferrazza, and R. D'Andrea, "Towards vision-based robotic skins: a data-driven, multi-camera tactile sensor," in *2020 3rd IEEE International Conference on Soft Robotics (RoboSoft)*. IEEE, 2020, pp. 333–338.
[35] J. Bewley, G. P. Jenkinson, and A. Tzemanaki, "Optical-tactile sensor for lump detection using pneumatic control," *Frontiers in Robotics and AI*, vol. 8, p. 672315, 2021.
[36] W. Yuan, S. Dong, and E. H. Adelson, "Gelsight: High-resolution robot tactile sensors for estimating geometry and force," *Sensors*, vol. 17, no. 12, p. 2762, 2017.
[37] D. F. Gomes, Z. Lin, and S. Luo, "Geltip: A finger-shaped optical tactile sensor for robotic manipulation," in *2020 IEEE/RSJ International Conference on Intelligent Robots and Systems (IROS)*. IEEE, 2020, pp. 9903–9909.
[38] H. Jiang, Y. Yan, X. Zhu, and C. Zhang, "A 3-d surface reconstruction with shadow processing for optical tactile sensors," *Sensors*, vol. 18, no. 9, p. 2785, 2018.
[39] Y. Zhang, X. Chen, M. Y. Wang, and H. Yu, "Multidimensional tactile sensor with a thin compound eye-inspired imaging system," *Soft Robotics*, vol. 9, no. 5, pp. 861–870, 2022.

Emmanuel Bacher is a research engineer at the Franco-German Research Institute of Saint-Louis (ISL), France. He received a Higher National Diploma in Electrical and Industrial Computer Science from the University of Haute-Alsace in Mulhouse, France, in 1993 and an M.Sc. in Experimental Physics from the Conservatoire national des arts et métiers, France, in 2001. Mr. Bacher is a team member in the Advanced Visionics and Processing group and is responsible for conducting experimental trials, automating experimental equipment, and designing integrated electronic circuits.

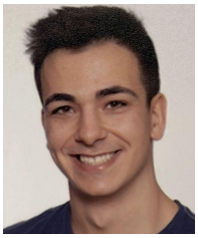

Sergio Cartiel obtained his Master's degree in Robotics, Graphics and Computer Vision at the University of Zaragoza in 2024. He is currently a Junior Researcher in the Graphics and Imaging Lab at the University of Zaragoza. His main research interests are light transport simulation, including time-resolved light transport, computational imaging and adaptive numerical integration methods.

Jorge García-Pueyo is a Junior Researcher in the Graphics and Imaging Lab at the University of Zaragoza. His main research interests are light transport simulation, including time-resolved light transport, and computational imaging, with focus on forward and inverse problems. He earned his Master's degree in Robotics, Graphics and Computer Vision at the University of Zaragoza in 2024.

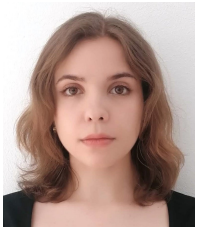

Julija Stopar obtained her Master's degree in Electrical Engineering at the University of Ljubljana in 2023. She is currently employed as a researcher at the Laboratory of Robotics within her alma mater. Her research interests lie primarily in the field of artificial intelligence, robotics, and information communication technologies.

Aleš Zore obtained his Master's degree in Electrical engineering in 2017 and is currently a researcher at Faculty of electrical engineering at University of Ljubljana. His latest research focuses are development of adaptive robotic cell and development of SoftSkin for human-robot enhanced safety.

Roman Kamnik received the D.Sc degree in electrical engineering from University of Ljubljana, Faculty of Electrical Engineering, Ljubljana, Slovenia, in 1999. He is currently a senior researcher in the Laboratory of Robotics and Full Professor at Faculty of Electrical Engineering, University of Ljubljana. His research interests are focused to the biomedical engineering and robotics. He is specialized in the development of intelligent robotic devices with the applications in sport, industrial and rehabilitation robotics, and transport.

Ilze Aulika is a leading researcher at ISSP UL and a solid-state physicist (PhD from the University of Latvia (UL) in 2008) with a diverse background in research and industry, with expertise in experimental physics, material science, and thin film technologies. She is one of the ToF based optical tactile sensor inventors; underpinned the Sestosenso project (GA number 101070310) to realize this concept jointly with ISL, UZ and UL. Current research: in-situ optical investigations of thin films/multilayers for smart windows and OLEDs, IR light interaction with the matter for ToF advanced applications.

Andrejs Ogurcovs earned his PhD in 2017 from Daugavpils University, specializing in solid-state physics. He is a researcher at ISSP UL. Research focus: development of metal-oxide nanostructure-based electrochemical sensor systems for detecting organic and inorganic substances and optical tactile transduction based on ToF investigations. Expertise: proficient in atomic force microscopy, electrochemistry, hydrothermal synthesis, and electronic hardware/software design for biosensor and optical skin applications.

Jurģis Grūbe , a leading researcher at the ISSP UL, obtained his PhD in 2005 with a specialization in solid-state spectroscopy. His research primarily focuses on up-conversion luminescence in diverse materials, including micro- and nanoparticles. He investigates luminescence decay kinetics and explores energy-transfer mechanisms that contribute to luminescence. Expertise: luminescence and exciton spectroscopy, absorption, transmission, reflectance spectra, spectroscopic experimental setups design.

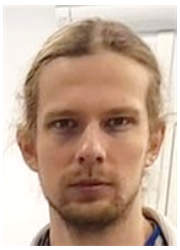

Arturs Bundulis , a senior researcher at ISSP UL (PhD from UL in 2020), specializes in 2nd/3rd-order nonlinear optical (NLO) studies of organic materials and their application in integrated photonics. His research encompasses structure-property relations, fundamental aspects of nonlinear effects, and NLO properties of plasmonic structures for photonic applications. Notably, he works on development of integrated polymer photonics based on host-guest systems for frequency comb and quantum light source development.

Jelena Butikova received her PhD in solid state physics in 2009 at the UL. She is a senior researcher at the Laboratory of Spectroscopy at the ISSP UL. She is responsible of the spectroscopic ellipsometer (SE), and she has experience in SE and expertise in laser spectroscopic methods.

Meldra Kemere received her PhD in Natural Sciences with a specialization in solid-state spectroscopy at the UL in 2023. She is a researcher at ISSP UL, Laboratory of Spectroscopy. She has experience in the optical characterization of various materials including glass-ceramics, polycrystalline, and polymer materials. Her expertise comprises luminescence and time-resolved measurements, and characterization of light transmission and reflection in materials.

Adolfo Muñoz is an Associate Professor at the Departament of Computer Science and Systems Engineering at Universidad de Zaragoza. In April 2010 he defended his PhD thesis "Light Transport in Participating Media" which established his original research topics: light transport simulation and capture and modeling of material appearance. More recently he has incorporated other interests such as computational and transient imaging. He belongs to the Graphics and Imaging Lab.

Martin Laurenzis graduated in physics from TU Dortmund University in 1999 and obtained his PhD in electrical engineering and information technology from RWTH Aachen University in 2005. Since 2004, he has been working at the Franco-German Research Institute Saint-Louis (ISL) in Saint-Louis, France, and is currently a Senior Research Fellow. After working on semiconductor electronics and optical data storage, his research interests turned to laser-based imaging, with a focus on 3D imaging, computational imaging techniques such as non-line-of-sight (NLOS) imaging and the application of single photon countering devices.).